

Conditionally Exponential Prior in Focal Near- and Far-Field EEG Source Localization via Randomized Multiresolution Scanning (RAMUS)

Joonas Lahtinen^{1a} ✉ · Alexandra Koulouri^{1a} · Atena Rezaei^a · Sampsä Pursiainen^a

Received: date / Accepted: date

Abstract This paper develops mathematical methods for localizing focal sources at different depths based on the non-invasive electro-/magnetoencephalography measurements. In the context of hierarchical Bayesian modelling, we introduce a conditionally exponential prior (CEP) which extends the concept of the conditionally Gaussian prior (CGP) and has been proposed to be advantageous in reconstructing far-field activity, in particular, when coupled with randomized multiresolution scanning (RAMUS). An approach to obtain the shape and scale parameter of the gamma hyperprior steering the CEP is derived from the physiological *a priori* knowledge of the brain activity. The core concept of this study is to show that the first-degree CEP will yield and improve the focality compared to the second-order case. The results of the present numerical experiments suggest that sources reconstructed via a combination of the first-degree CEP and RAMUS achieve an accuracy comparable to the second-degree case while being more focal for nu-

merically simulated originators of human somatosensory evoked potentials (SEPs) related to human median nerve stimulation, including simultaneous thalamic and cortical activity, as well as for a sub-thalamic dipolar and quadrupolar source configuration.

Keywords Brain imaging · EEG · Hierarchical Bayesian model · Randomized multiresolution scanning

1 Introduction

This paper aims to advance the mathematical tools for localizing focal sources at different depths based on non-invasive electro-/magnetoencephalography (EEG-/MEG) measurements [16, 25]. The EEG/MEG source localization task (using distributed source modelling) is an ill-posed inverse problem [16] a.k.a. it is not uniquely solvable and is sensitive to different modelling and measurement errors. Consequently, only a slight amount of noise in the measurement can significantly affect the reconstruction found by the inversion algorithm. This is especially the case for the far-field activity components, e.g., sub-cortical activity. The feasibility of depth-localization with non-invasive measurements has been suggested recently in studies concentrating on high-density measurements and filtering aspects [33, 29]. Our focus here is methodological. That is, we propose to enhance the detectability of both cortical and sub-cortical activity via im-

¹ J.L. and A.K. contributed equally to this study.

Joonas Lahtinen
E-mail: joonas.j.lahtinen@tuni.fi

Alexandra Koulouri
E-mail: alexandra.koulouri@tuni.fi

Atena Rezaei
E-mail: atena.rezaei@tuni.fi

Sampsä Pursiainen
E-mail: sampsä.pursiainen@tuni.fi

^aComputing Sciences, Faculty of Information Sciences, Tampere University, Korkeakoulunkatu 1, 33014 Tampere

proving the mathematical method to reconstruct the sources. For simplicity, we concentrate here on the case of EEG, while the present methodology is also directly applicable in the case of MEG [8].

With this study, our aims are first by employing the hierarchical Bayesian modelling (HBM) to develop optimization problems that allow reconstructing focal or distributed brain activity at different depths and then compare different reconstruction algorithms to solve them. To this end, we extend the well-known concept of the conditionally Gaussian prior (CGP) [8] by introducing a conditionally exponential prior (CEP), i.e., an exponential power distribution also referred to as a generalized normal distribution [24] which includes a q -norm in the exponent. Through the hierarchical prior structure, our formulation allows to take into account the physical and physiological properties of the underlying primary currents which we, in this study, apply to fix the shape and scale parameter steering of the gamma hyperprior for the CEP.

In this paper, we show mathematically how the HBM approach previously introduced in [8] can be extended to the case of the CEP and how the resulting statistical framework can be associated with the previously described CGP model. As shown in [31], the numerical implementation of the method is an important factor contributing the eventual performance of the inverse model. Therefore, we compare two alternative techniques for maximizing the posterior. Firstly, we present an expectation maximization (EM) based approach to find an optimized reconstruction and, secondly, show that, when applying the Lasso algorithm [35], it is similar to the IAS maximum a posteriori (MAP) estimation technique of [8]. The equivalence of these approaches is presented in the case of $q = 2$. The main difference between EM and IAS reconstructions is that the candidate optimizer is updated by finding the mean and mode of the hyperparameter, respectively. Furthermore, the randomized multiresolution scanning (RAMUS) approach is applied as a necessary technique to discretize the source space so that both near- and far-field sources can be distinguished [31].

We analyze the present CEP model in numerical experiments in which we consider reconstructing the cortical and sub-cortical activity producing the somatosensory evoked potential (SEP) of the median nerve stimulation [25]. The early components occur ≤ 20 ms post-stimulus involve sub-cortical far-field activity, i.e., activity far from the electrodes, which we here simulate and reconstruct numerically utilizing the CEP model together with a realistic head model segmentation. We consider especially the P14/N14, P16/N16 and P20/N20 component, i.e., the positive (P) and negative (N) 14, 16 and 20 ms post-stimulus peaks in the measured data with respect to the forehead potential. As a forward modelling technique, we apply the finite element method (FEM) [21, 30, 22] which is advantageous in the present application, since it, as a volumetric technique, allows decomposing the head model into multiple highly accurate cortical and sub-cortical compartments.

The results obtained suggest that the first-degree CEP provides a crucial approach to detect focal near- and far-field activity in connection with the RAMUS technique. Namely, while CEP and CGP yield a similar source localization accuracy, the activity reconstructed via the first-degree CEP is overall more well-localized compared to CGP. This was found to be the case for simultaneous thalamic and cortical activity, approximating the originator of P20/N20, as well as for a sub-thalamic dipolar or quadrupolar source corresponding to the potential originators of P14/N14 and P16/N16 [7], respectively.

This article is organized as follows. In Section 2 we present a generalized exponential prior model to HBM based source localization as well as the EM and IAS algorithms. Section 2 concentrates on the implementation of this methodology. The results are presented in Section 4 and discussed in Section 5. Finally, Section 6 concludes the study.

2 Hierarchical Bayesian framework for a conditionally exponential prior

We consider the EEG observation model

$$\mathbf{y} = \mathbf{L}\mathbf{x} + \mathbf{e}, \quad (1)$$

where $\mathbf{x} \in \mathbb{R}^n$, $\mathbf{y} \in \mathbb{R}^m$ and $\mathcal{N}(\mathbf{e}; 0, \sigma^2)$ with σ a scale-invariant prior. From Bayes' rule we have $\pi(\mathbf{x} | \mathbf{y}) \propto \pi(\mathbf{y} | \mathbf{x})\pi(\mathbf{x})$. The unknown \mathbf{x} represents the discretized primary current distribution \mathbf{J} (vector field) of the neural activity. At a given position, \mathbf{J} is described by a three-component vector or, equivalently, three entries of \mathbf{x} . Given the likelihood function $\pi(\mathbf{y} | \mathbf{x}) \propto \exp(-\frac{1}{2\sigma^2}\|\mathbf{L}\mathbf{x} - \mathbf{y}\|_2^2)$ and a subjectively selected prior $\pi(\mathbf{x})$, the posterior $\pi(\mathbf{x} | \mathbf{y})$ is assumed to contain all the information about the underlying source activity. We associate each source x_i with an exponential power distribution

$$\pi(x_i, 1/\gamma_i, q) \propto \gamma_i^{1/q} \exp(-\gamma_i|x_i|^q) \quad (2)$$

determined by the hyperparameter γ_i and the degree q of the prior, which is selected to be either one or two in this study. Selecting between $q = 1$ and $q = 2$ allows one to steer the focality of the reconstruction, since the exponential distribution can be justified to be more heavy-tailed in the former case (i.e. Laplace distribution). By introducing an extra level of hierarchy in this prior (2), we aim to obtain a minimization problem that allows reconstructing more focal, intensity unbiased or deeper sources, as suggested in [8, 31], compared to the minimization problem that employs a fixed γ_i together with the Laplace prior, when $q = 1$, or the standard Gaussian prior, when $q = 2$. Consequently, the current analysis belongs to the hierarchical Bayesian adaptive framework introduced, e.g., in [23]. In particular, with γ_i being a random variable following a Gamma hyperprior distribution, i.e., $\gamma_i \sim \text{Ga}(\kappa, \theta)$ for $i = 1, \dots, n$, $\pi(\gamma_i|x_i)$ is also a Gamma distribution, that is, $\gamma_i|x_i \sim \text{Ga}(\gamma_i|x_i; \kappa + 1/q, \theta + |x_i|^q)$ by conjugacy. The full posterior obeying a CEP

$\pi(\mathbf{x} | \gamma)$ is given by

$$\begin{aligned} \pi(\mathbf{x}, \gamma | \mathbf{y}) &\propto \pi(\mathbf{y} | \mathbf{x}) \pi(\mathbf{x} | \gamma) \pi(\gamma) \\ &= \pi(\mathbf{y} | \mathbf{x}) \prod_{i=1}^n \pi(x_i | \gamma_i) \pi(\gamma_i), \end{aligned} \quad (3)$$

where $\pi(\mathbf{x} | \gamma)$ and $\pi(\gamma)$ correspond to the CEP following from (2) and the hyperprior, respectively. In the following subsections, we use two different approaches to estimate the mode of the marginal posterior $\pi(\mathbf{x} | \mathbf{y})$ given the CEP. The first one relies on EM and the second one on IAS [10, 8, 9].

2.1 EM for the hierarchical adaptive framework

The EM-based maximum a posteriori (MAP) estimate is given by the system

$$\begin{aligned} \hat{\mathbf{x}}^{(j+1)} &= \arg \min_{\mathbf{x}} \left\{ -\frac{1}{2\sigma^2} \|\mathbf{L}\mathbf{x} - \mathbf{y}\|_2^2 \right. \\ &\quad \left. + \mathbb{E}_{\pi(\gamma|\hat{\mathbf{x}}^{(j)})} [\log \pi(\mathbf{x} | \gamma)] \right\}, \end{aligned} \quad (4)$$

where the expectation of $\log \pi(\mathbf{x} | \gamma)$ with respect to the conditional probability density $\pi(\gamma|\hat{\mathbf{x}}^{(j)})$ and $\pi(\gamma_i|\hat{x}_i^{(j)})$ given the MAP estimate $\hat{\mathbf{x}}_i^{(j)}$ for $i = 1, \dots, n$ is

$$\begin{aligned} \mathbb{E}_{\pi(\gamma|\hat{\mathbf{x}}^{(j)})} [\log \pi(\mathbf{x} | \gamma)] &= \sum_{i=1}^n \mathbb{E}_{\pi(\gamma_i|\hat{x}_i^{(j)})} [\log \pi(x_i | \gamma_i)] \\ &= \sum_{i=1}^n \int_0^\infty \pi(\gamma_i|\hat{x}_i^{(j)}) \log \pi(x_i | \gamma_i) d\gamma_i \\ &= -\sum_{i=1}^n |x_i|^q \int_0^\infty \gamma_i \pi(\gamma_i|\hat{x}_i^{(j)}) d\gamma_i + C, \end{aligned} \quad (5)$$

with $\mathbb{E}_{\pi(\gamma_i|\hat{x}_i^{(j)})} [\gamma_i] = \int_0^\infty \gamma_i \pi(\gamma_i|\hat{x}_i^{(j)}) d\gamma_i = \frac{\kappa+1/q}{\theta+|\hat{x}_i^{(j)}|^q}$. Therefore, we have the following optimization problem:

$$\begin{aligned} \tilde{\gamma}_i^{(j)} &= \frac{\kappa + 1/q}{\theta + |\hat{x}_i^{(j)}|^q} \text{ for } i = 1, \dots, n \\ \hat{\mathbf{x}}^{(j+1)} &= \arg \min_{\mathbf{x}} \left\{ \frac{1}{2\sigma^2} \|\mathbf{L}\mathbf{x} - \mathbf{y}\|_2^2 + \sum_{i=1}^n \tilde{\gamma}_i^{(j)} |x_i|^q \right\}. \end{aligned} \quad (6)$$

When $q = 1$, this resembles the Lasso problem which, expressed through (17), corresponds to a Laplace prior (14) with a fixed γ_i .

Notice that EM (6) finds the MAP estimate using as prior the marginal distribution of x_i , i.e., $\pi(x_i) = \int_{\gamma_i} \pi(x_i|\gamma_i) \pi(\gamma_i) d\gamma_i$,

$$\pi(x_i; \kappa, \theta, q) \propto \left(\frac{|x_i|^q}{\theta} + 1 \right)^{-(\kappa+1/q)}, \quad (7)$$

where κ and θ are the shape and scale parameter of $\text{Ga}(\gamma_i; \kappa, \theta)$, respectively. This distribution exhibits very heavy tails, meaning that some realizations x_i will be much greater in magnitude than its expectation. Consequently, this prior tends to favor sparse estimates for \mathbf{x} . This tendency is enhanced in the exponential prior (2) via the hierarchical prior structure, especially, when $q = 1$ compared to $q = 2$ [23, 27].

2.2 Iterative Alternating Sequential algorithm

In IAS, we aim at estimating the MAP of the pair (x, γ) by solving the optimization problem $(\hat{\mathbf{x}}, \hat{\boldsymbol{\gamma}}) = \arg \max_{\mathbf{x}, \boldsymbol{\gamma}} \pi(\mathbf{x}, \boldsymbol{\gamma} | \mathbf{y})$. A common procedure [27] is to evaluate it via alternating optimization with respect to \mathbf{x} and $\boldsymbol{\gamma}$. In particular, the MAP estimates can be extracted by solving alternately and recursively the following two optimization problems

$$\begin{aligned} \hat{\boldsymbol{\gamma}}^{(j)} &= \arg \max_{\boldsymbol{\gamma}} \log \pi(\boldsymbol{\gamma} | \mathbf{y}, \hat{\mathbf{x}}^{(j)}), \\ \hat{\mathbf{x}}^{(j+1)} &= \arg \max_{\mathbf{x}} \log \pi(\mathbf{x} | \mathbf{y}, \hat{\boldsymbol{\gamma}}^{(j)}). \end{aligned} \quad (8)$$

To express explicitly the two previous optimization problems, we write the full posterior $\pi(\mathbf{x}, \boldsymbol{\gamma} | \mathbf{y})$ which is

$$\begin{aligned} \pi(\mathbf{x}, \boldsymbol{\gamma} | \mathbf{y}) \propto \exp \left(- \frac{1}{2\sigma^2} \|\mathbf{L}\mathbf{x} - \mathbf{y}\|_2^2 \right. \\ \left. - \sum_{i=1}^n (\gamma_i (|x_i|^q + \theta) - (1/q + \kappa - 1) \log \gamma_i) \right). \end{aligned} \quad (9)$$

It follows that the optimization problem (8) can be written as

$$\begin{aligned} \hat{\gamma}_i^{(j)} &= \frac{\kappa + 1/q - 1}{|\hat{x}_i^{(j)}|^q + \theta} \text{ for } i = 1, \dots, n, \\ \hat{\mathbf{x}}^{(j+1)} &= \arg \min_{\mathbf{x}} \left\{ \frac{1}{2\sigma^2} \|\mathbf{L}\mathbf{x} - \mathbf{y}\|_2^2 + \sum_{i=1}^n \hat{\gamma}_i^{(j)} |x_i|^q \right\}. \end{aligned}$$

(10)

2.3 Difference between EM and IAS approaches

One can observe that the difference between the problems of (6) and (10) is the update of the γ parameter. In EM algorithm, the update of γ_i is based on the estimation of the expectation of γ_i (see 4) whereas in IAS, the update comes from the mode of $\pi(\gamma_i|x_i)$. Since we have that $\gamma_i|x_i \sim \text{Ga}(\gamma_i; \kappa + 1/q, \theta + |x_i|^q)$, we saw that the two updates can be explicitly expressed. In this article, we investigate how the prior degree $q = 1$ or $q = 2$ affects the source reconstructions and how the mode or expectation of γ_i as updating rules influence the performance of an EEG source localization solver.

3 Implementation

The EM and IAS approaches to posterior maximization were implemented as external packages (plugins) of the Matlab based *Zeffiro interface* (ZI) code package [18] which allows for using the detailed multi-compartment head models obtained via high resolution magnetic resonance imaging (MRI) data. ZI's plugin has its own user interface and an access to all the variables, parameters and handles. ZI utilizes the volumetric finite element method (FEM) [22] in the forward modelling stage which is why both cortical and sub-cortical compartments can be modelled accurately without limiting their number.

3.1 Discretization and source model

In ZI, a given head model is discretized using a tetrahedral finite element (FE) mesh. One-millimeter mesh resolution [32] is applied in order to achieve a high enough accuracy with respect to the strongly folded tissue structure of the brain and thin layers of the skull. The source space is modelled via the divergence conforming approach [21] in which the primary current density of the brain activity is formed by a superposition of dipole-like sources belonging to the Hilbert

space $H(\text{div})$ of vector fields with a square (L_2) integrable divergence [2]. The $H(\text{div})$ model is advantageous, since it enables the accurate modelling of both well-localized dipolar and realistic distributed sources and, in especially, since analytical dipoles are inapplicable (singular) as sources of the FEM forward simulation. In ZI, the $H(\text{div})$ sources are distributed evenly (randomly and uniformly) in the active compartments of the head model. The mesh-based source orientations following from the FEM discretization are interpolated into Cartesian directions using the position based optimization approach [1] in the case of the 10-point stencil [30] in which the source contained by a center tetrahedron is modelled by six edge-wise and four face-intersecting sources associated with the edges and faces of that tetrahedron. Each source position is associated with the three Cartesian source orientations. The source distribution of the cerebral cortex was assumed to be parallel to its local surface normal due to the normally oriented axons of the cortex [12]. This normal constraint was implemented by projecting the Cartesian source field to the nearest surface normal direction in the grey matter compartment. The source orientations of the other compartments were unconstrained.

3.2 Randomized multiresolution scanning (RAMUS)

The RAMUS technique was applied in finding a MAP estimate in order to maximize the robustness of the source localization outcome for various source depths [31]. That is, each MAP estimate was found for a large number of subsets of the source space and the final estimate was found as the average of all these subset-based estimates. In RAMUS, each subset contains a given number of randomly and uniformly distributed source positions. These subsets are divided to resolution levels according to the source position count. The estimates are evaluated in an ascending order with respect to the resolution, i.e., progressing from coarse (sparse) to fine resolutions. Furthermore, the estimate obtained at one resolution level is used as the initial guess for the next one. The presence of coarse resolu-

tions can be shown to be essential, specially, regarding the distinguishability of the deep activity [20], whereas finer resolutions can provide an enhanced accuracy for the detection of the near-field (cortical) activity. The average estimate found for a randomized set of source sub-spaces with a given number of sources provides an enhanced robustness for each resolution, as it diminishes discretization and modelling errors [31]. In this study, each source set in the coarsest resolution level includes 10 source positions and the source count is multiplied by the factor of 10 (sparsity factor) when moving up by one resolution level in the multiresolution hierarchy. The results were averaged over 100 different multiresolution decompositions.

3.2.1 Source localization experiments with spherical model

The quantitative performance of the EM and IAS techniques was analyzed using the isotropical Ary model which consists of three concentric spherical compartments modelling the brain, skull and skin. The radii of these layers are 82, 86 and 92 mm and their electrical conductivities are 0.33, 0.0042, and 0.33 S/m, respectively. A spherical model is used in order to minimize the effect of tissue structure on the source localization accuracy. The Ary model was discretized using one-millimeter accuracy and the source space within the brain compartment consisted of 10000 source positions.

Accuracy measures

The source localization accuracy with respect to a given dipolar source was investigated by comparing its position, orientation and amplitude to the corresponding integral means obtained for the reconstructed distribution. Each integral mean was calculated with respect to a 30 mm radius region of interest (ROI) centered at the source position. The following measures were evaluated: (1) the Euclidean distance and (2) angle (degrees) difference, and (3) the amplitude ratio between the reconstructed and actual source.

Focality measures

We consider three different focality measures described in the following. (1) Hard thresholding is calculated by dividing the number of the source positions, where the reconstruction is larger than 75 % of its maximum within the ROI, by the number of sources inside the ROI. (2) The coefficient of variation (CV), a statistical measure of dispersion, is obtained as the ratio of the standard deviation to the mean evaluated in the set of source positions. Here it is applied as a possible statistical interpretation of the focality. Statistical dispersion is a relative measure of variability of the given data. Due to the fact that the brain activity can be seen as the outlier of the current density data, CV will be higher when activity is focal. We have chosen CV, because it can estimate dispersion even for very slightly dispersed data and the results from different data sets are comparable to each other. (3) The mean spatial focality (MSF) measure is defined here as the average Euclidean distance $F = \frac{1}{|\mathcal{S}|} \sum_{j \in \mathcal{S}} \|\vec{p}_j - \langle \vec{p} \rangle_{\mathcal{S}}\|_2$ between the mean position $\langle \vec{p} \rangle_{\mathcal{S}} = \sum_{i \in \mathcal{S}} \vec{p}_i / |\mathcal{S}|$ of the high value cloud \mathcal{S} with $\mathcal{S} = \{i: \|\mathbf{J}(\vec{p}_i)\|_2 \geq \epsilon \max_j \{\|\mathbf{J}(\vec{p}_j)\|_2\}\}$, where $\|\mathbf{J}(\vec{p}_i)\|_2$ denotes the intensity of the three-component current density field reconstructed at the i -th source position \vec{p}_i . In \mathcal{S} , the norm of the reconstructed field is set to be greater than 75 % of its maximum value, i.e., ($\epsilon = 0.75$). The definition of MSF means in practice that we estimate the location of the estimation peak in the ROI and calculate its mean distance to source points that have a high weight. This gives a measure that is proportional to the diameter of the high value cloud.

3.2.2 Source localization experiments with MRI-based model

In the qualitative analysis, we use a multi-compartment segmentation generated using open T1-weighted MRI data obtained for a healthy subject. Using this data, a surface segmentation was generated using the FreeSurfer software suite. The ASCII-format surface meshes generated using FreeSurfer were then imported to ZI,

where a regular tetrahedral mesh with a one-millimeter accuracy was generated. The number of individual source positions was selected to be 100000. The tissue conductivities suggested in [13] were applied, i.e., 0.14, 0.33, 0.0064, 1.79, and 0.33 S/m for the white and grey matter, skull, cerebrospinal fluid (CSF), and skin, respectively. In addition to these compartments, a set of sub-cortical compartments were included in the model. The conductivity of those was assumed to be 0.33 S/m.

3.2.3 EM and IAS estimates

To analyze the accuracy and focality of the EM and IAS source localization estimates, we generated a sample of 50 different noise vector realizations utilizing the model of zero mean Gaussian noise with 3 % or 5 % relative standard deviation with respect to the entry with the largest absolute value in the simulated noiseless data vector. Applying these noise realizations, a sample of EM and IAS estimates was obtained for source configuration **(I)**–**(III)** evaluating the accuracy and focality measures for each estimate. Following the findings of [31, 8], the number of iterations applied to find a reconstruction was chosen to be 10. The number of the Lasso iteration steps applied in finding $\hat{\mathbf{x}}^{(j+1)}$ in (17) and (10) with $q = 1$ was chosen to be 5.

3.3 Physiology-based parameter choice

To select the shape and scale parameter of the hyperprior, we choose the expectation $\mathbb{E}_{\pi(x_i; \kappa, \theta, q)[x_i]}$ of the marginal prior (7), that gives the expected deviation for every component x_i of the reconstruction vector, to match approximately with the amplitude of the expected random fluctuations in the reconstruction, and the actual brain activity to be found will appropriately correspond to the tail part, i.e., it is an outlier with respect to the noise level. Due to the linear forward model, the noise level of the reconstruction may be assumed to be roughly that of the noise. Thus, a random fluctuation may be assumed to have an amplitude of the relative measurement noise standard deviation

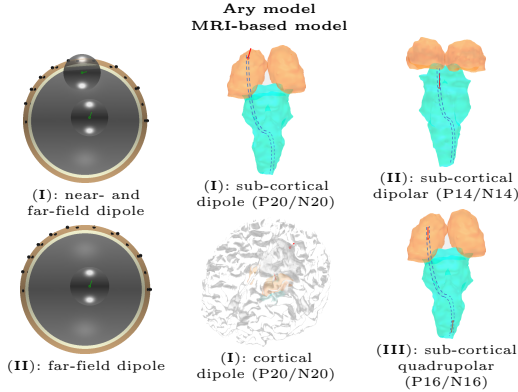


Fig. 1: Visualization of near- (cortical) and far-field (sub-cortical) source placement in the spherical Ary (1st from the left) and MRI-based head model (2nd and 3rd from the left). Each source position and orientation is depicted by a pointer (green for Ary, red for MRI-based model) which, in the case of Ary, is surrounded by a sphere showing the extent of the corresponding ROI. Configuration (I) corresponding to P20/N20 component of the median nerve SEP includes a superficial and deep dipole which in the MRI-based model are located in the ventral posterolateral (VPL) thalamus (top row) and in the Brodmann area 3b of the primary somatosensory cortex (bottom row), respectively. The cortical source inherits its normal orientation with respect to the cortical surface (here the white matter surface) from that of the cortical neurons. The thalamic source is oriented along the dorsal column–medial lemniscus pathway (blue dash) which is a bundle of basically vertical neuron fibers conducting the SEP from the median nerve through the brainstem and thalamus to the primary somatosensory cortex. A single upward-pointing deep dipole constitutes configuration (II) based on the P14/N14 component. In the MRI-based model, it is located in the upper part of the brainstem, especially, in the medial lemniscus. Configuration (III) is quadrupolar, i.e., a combination of two oppositely oriented dipoles, a ventrolateral thalamic dipole with an upward orientation and a dipole in the cuneate nucleus with an opposite orientation, creating the positive and negative pole of P16/N16 [19], respectively.

(here 3 or 5 %) multiplied by a typical dipolar primary current amplitude in the brain, e.g., 10 nAm (1E-8 Am) [16]. By taking into account that the largest absolute value in the measurement data is set to one microvolt which is a typical EEG measurement amplitude [25] and the lead field matrix is presented in SI-units, we can conclude the relative noise level of reconstruct-

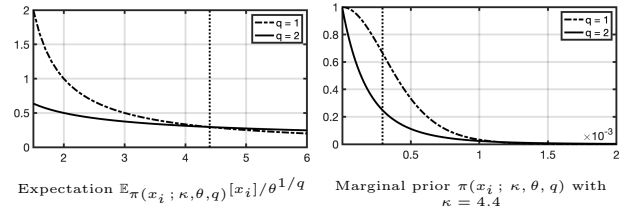


Fig. 2: **Left:** The ratio between the expectation $\mathbb{E}_{\pi(x_i; \kappa, \theta, q)}[x_i]$ of the marginal prior and $\theta^{1/q}$ as a function of the shape parameter value κ from $\kappa = 1.5$ to $\kappa = 6$. The vertical line corresponds to the value $\kappa = 4.4$ for which the cases $q = 1$ and $q = 2$ match. **Right:** The marginal prior (normalized to one) with the expectation set to $3\text{E-}4$, approximating typical deviations due to noise. The shape parameter is $\kappa = 4.4$ and the scale parameter $\theta = 1\text{E-}3$, when $q = 1$, and $\theta = 1\text{E-}6$, when $q = 2$, resulting into $\mathbb{E}_{\pi(x_i; \kappa, \theta, q)}[x_i] = 3\text{E-}4$ in both cases. With these parameter choices the expectation can be assumed to appropriately coincide with the amplitude of the expected random fluctuations of the reconstruction and the intensity of the actual source to be found is located in the tail part, i.e., it is an outlier with respect to the noise level (Section 3.3).

tion to be $\alpha \cdot 1\text{E-}8 \cdot 1\text{E}6$ in micro units, where α is the standard deviation of the Gaussian noise associated with the likelihood. If we choose 3 % as the likelihood, it follows that the considered expectation of deviation is $3\text{E-}4$. The shape parameter is chosen to be $\kappa = 4.4$ for which the ratio between $\mathbb{E}_{\pi(x_i; \kappa, \theta, q)}[x_i]$ and $\theta^{1/q}$ is equal for both prior degrees $q = 1$ and $q = 2$, i.e., $\frac{\mathbb{E}_{\pi(x_i; \kappa, \theta, q)}[x_i]}{\theta^{1/q}} \Big|_{q=1} = \frac{\mathbb{E}_{\pi(x_i; \kappa, \theta, q)}[x_i]}{\theta^{1/q}} \Big|_{q=2} \approx 0.3$. In this way, we try to reduce the effect of the parameters in the comparison between prior degrees q . Consequently, the value of $\mathbb{E}_{\pi(x_i; \kappa, \theta, q)}[x_i]$ follows from the scale parameter which is set to be $\theta = 1\text{E-}3$ and $\theta = 1\text{E-}6$ for $q = 1$ and $q = 2$, respectively, in order to obtain the correspondence to the noise as described above.

3.3.1 Synthetic data of somatosensory evoked potentials

We consider the detection of a synthetic SEP of the human median nerve stimulation as an example case in the numerical experiments. The SEP propagates through the brainstem and thalamus to the somatosensory cortex, the Brodmann area 3b is located at the

posterior wall of the central sulcus, in which it is detectable 20 ms post-stimulus [5, 7, 4, 6]. This P20/N20 component originates principally in the 3b area, but involves also ipsilateral sub-cortical activity occurring in the ventral posterolateral (VPL) part of the thalamus at the same time [17]. P20/N20 is preceded by far-field components P14/N14 and P16/N16 occurring at 14 and 16 ms post-stimulus, respectively. P14/N14 originates in the brainstem, where the spike volley travels through medial lemniscus pathway which is known as a bundle of fibers [26]. The far-field activity for P16/N16 is modelled here as a quadrupole configuration including a positive thalamic and a negative sub-thalamic originator corresponding to the P16 and N16, respectively [19, 7]. The first one of these is located at the ventrolateral thalamus and the second one in the cuneate nucleus.

The following three configurations **(I)**–**(III)** of dipolar sources were applied to model the activity occurring at 14, 16 and 20 ms post-stimulus. Configuration **(I)** consists of two sources modelling the simultaneous near- (cortical) and far-field (thalamic) activity corresponding to P20/N20. The amplitude of the cortical source is assumed to be 70 % of the thalamic one, modelling a situation, where the amplitude of the cortical activity is intensifying before reaching its maximum. **(II)** is formed by a single source in the medial lemniscus approximating the deep-restricted activity of P14/N14. **(III)** includes a quadrupolar configuration with an upward component in the ventral thalamus and a downward component in the cuneate nucleus of the brainstem [19]. Since the thalamic component is likely to be peaked slightly after 16 ms [19], its amplitude is assumed to be 77 % compared to the amplitude of the sub-thalamic component. The present quadrupolar setup is not to be mixed with a quadrupolar afferent volley which is difficult to be detected as is. Instead the two dipolar components correspond to two subsequent quadrupolar spikes with one of the dipolar components visible due to a local discontinuity of the conductivity distribution [7].

A spherical and an MRI-based model were applied in the source localization tests. Configuration **(III)**

was applied only with the MRI-based model which allows distinguishing the thalamic and brainstem areas. With the first one of these, the source positions were selected according to [7, 4] and, in the second one, they were placed in the aforementioned originator areas (Figure 1). The noise vector \mathbf{e} in (1) was assumed to be zero-mean and Gaussian random variable with diagonal covariance and 3 % relative standard deviation compared to the amplitude of the noiseless signal.

4 Results

The accuracy and focality results obtained with the spherical Ary model are shown as histograms in Figures 3, 4 and 8, 9 for 3 and 5 % noise, respectively. The CEP prior model reconstructs the near- and far-field activity with both prior degrees $q = 1$ and $q = 2$ and reconstruction techniques EM and IAS. While the degree of the prior does not directly appear to affect the position and orientation accuracy, the reconstructions were overall more focal in the case $q = 1$ compared to $q = 2$. With $q = 1$ the reconstruction of the near-field source was more focal compared to that of the deep one, while with $q = 2$ such a tendency was less obvious or absent. Of the three focality measures, the clearest differences were obtained with the hard threshold measures. CV and MSF, are measuring the dynamical structure of the reconstructed distribution (Section 3.2.1), show similar tendencies as the hard threshold. Of these, CV reveal smaller relative differences, suggesting that the overall variation is rather similar, while the focality of the maximum peak varies more significantly. MSF shows a drastic difference between the near-field reconstructions obtained with the first- and second-degree CEP. When comparing the outcome of the EM and IAS reconstruction techniques, the differences between the EM and IAS approach are less obvious than those following from the depth of the source, the degree of the prior and the noise level.

The results obtained with the MRI-based head model are visualized in Figures 5–7 and in Figures 10–12 for 3 and 5 % noise, respectively. The first-degree CEP,

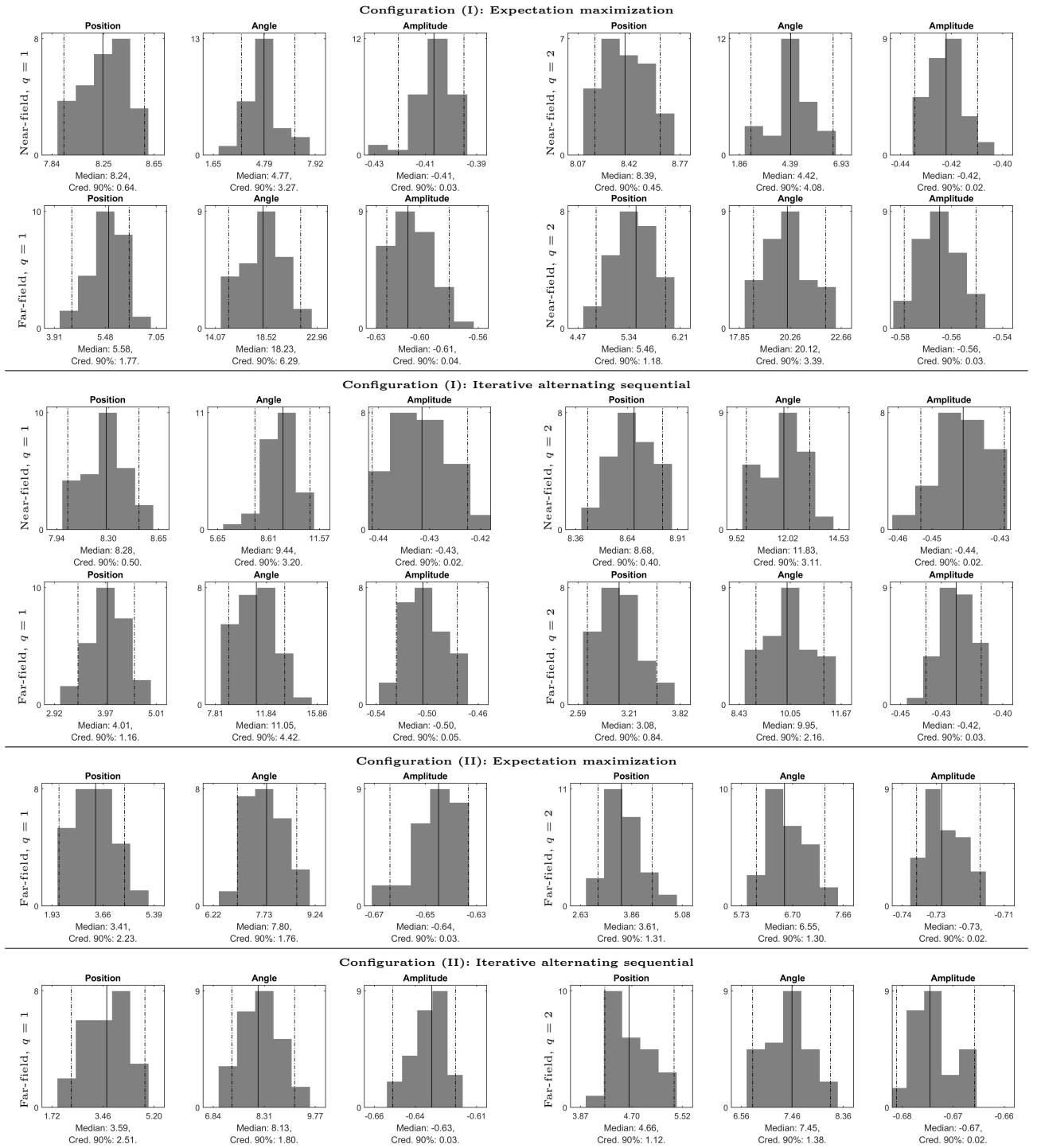


Fig. 3: The source localization accuracy measures (position, angle, amplitude, and maximum) which are evaluated in the spherical Ary model (Section 3.2.1) with 3 % noise for source configuration (I) and (II) applying the EM and IAS algorithm. The histograms show the results obtained for 50 different reconstructions each corresponding to a different realization of the measurement noise. The measures concern the difference between the actual source and the mass centre of the reconstructed distribution in the corresponding ROI. The units of the position, angle and amplitude are, respectively, in mm, degrees and $\log_{10}(A_r/A_s)$, where A_r is the amplitude of the reconstructed and A_s of the actual source.

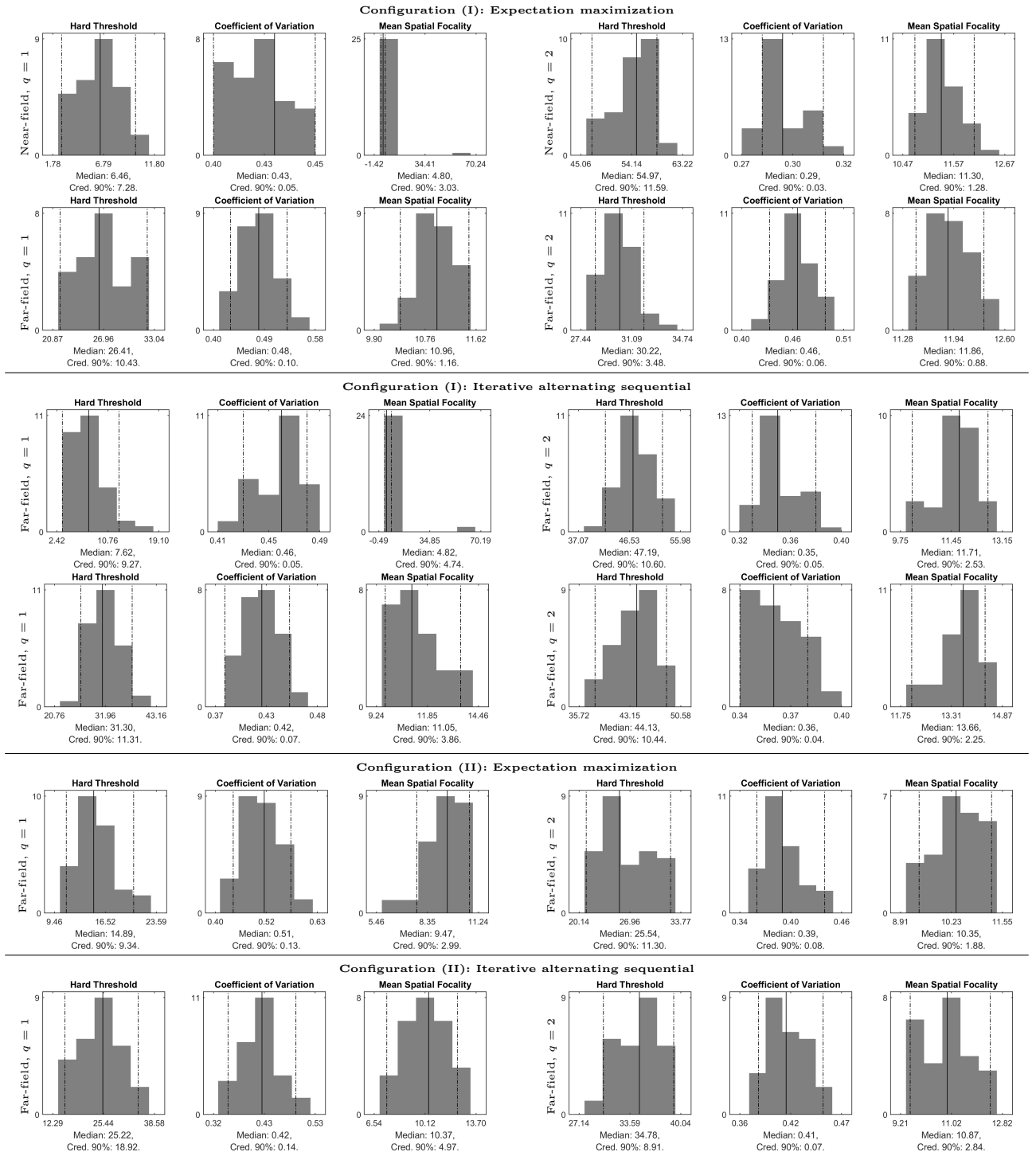


Fig. 4: The focalty measures evaluated in the spherical Ary model (Section 3.2.1) with 3 % noise for source configuration (I) and (II) applying the EM and IAS algorithm. The histograms show the results obtained for 50 different reconstructions each corresponding to a different realization of the measurement noise. The hard threshold measure concerns the area, where the intensity of the reconstruction is at least 75 % of its maximum in the corresponding ROI. The coefficient of variation (CV) and mean spatial focality (MSF) measure the dynamical distribution of the reconstruction as described in Section 3.2.1.

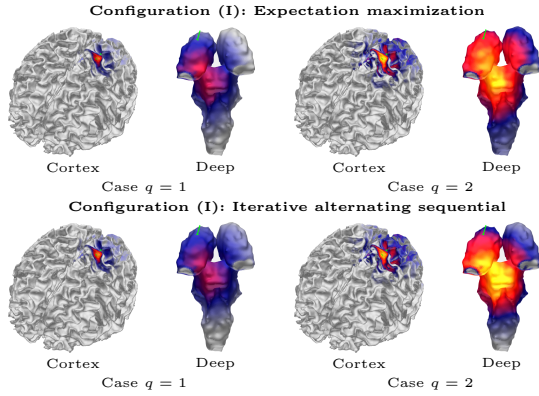


Fig. 5: The reconstructions obtained with the MRI-based head multi-compartment model with 3 % noise for source configuration **(I)** including two sources, one placed in the left 3b Brodmann area of the central sulcus, pointing inwards in the direction of the local surface normal vector, and a vertical source placed in the ventral posterolateral part of the left thalamus (Figure 1). The actual source position is visualized by a green pointer in each image. The first-degree conditionally exponential prior (CEP), i.e., the case $q = 1$, leads to a more focal reconstruction than the second-degree CEP ($q = 2$).

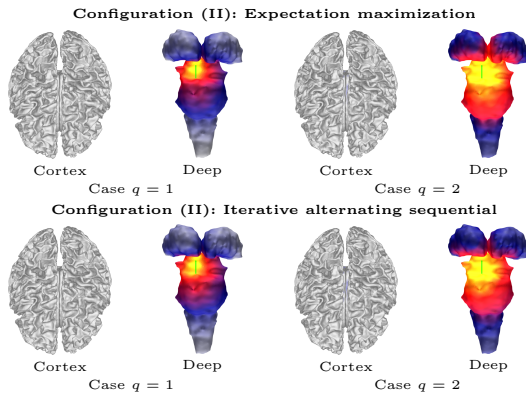


Fig. 6: The reconstructions obtained with the MRI-based head multi-compartment model with 3 % noise for source configuration **(II)**, including a single deep source placed in the brainstem (green pointer). The maximum found corresponds with the actual position, a similar amplitude is obtained with both $q = 1$ and $q = 2$, the focality being greater with $q = 1$. The EM and IAS reconstruction method were found to perform essentially similarly for both source configurations with the most significant differences in the deep component of configuration **(I)**.

i.e., the case $q = 1$, leads to an overall more focal reconstruction compared to $q = 2$. Akin to the results obtained for the Ary model, the near-field component,

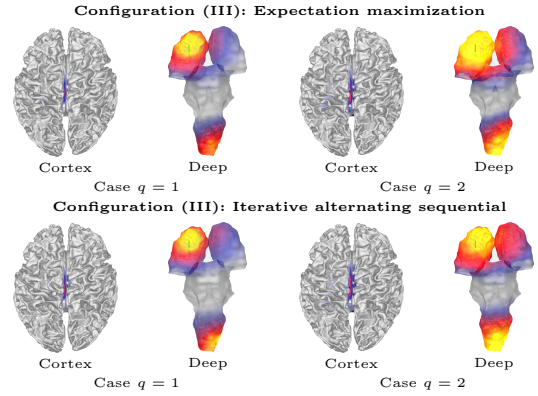


Fig. 7: The reconstructions obtained with the MRI-based head multi-compartment model with 3 % noise for source configuration **(III)** with a quadrupolar deep source configuration formed by two dipolar components, one in the ventral part of the left thalamus [7] and another one in lower medulla of the brainstem [19] (green arrows). The quadrupolar configuration is detected with both $q = 1$ and $q = 2$. The reconstruction obtained is more focal in the former case. .

i.e., the cortical pattern obtained with configuration **(I)** is more focal with $q = 1$ than with $q = 2$; in the former case it is clearly restricted to the Brodmann 3b area, whereas in the latter one it spreads more clearly to the more posterior areas, e.g., 5 and 7. Neither of the cases finds the accurate location of the simultaneous deep activity which appears more focal with $q = 1$. For the single-source configuration **(II)**, agreeing with the case of the Ary model, the maximum of the deep source found corresponds to the actual position and a similar amplitude is obtained with both $q = 1$ and $q = 2$, while in the former case, the distribution is more concentrated around the actual source position, distinguishing the upper brainstem as the area of activity. The EM and IAS reconstruction method were found to perform essentially similarly for both source configurations with the most significant differences in the deep component of the configuration **(I)**. For **(III)**, the thalamic and sub-thalamic component of the quadrupolar configuration are detected with both prior degrees $q = 1$ and $q = 2$, the results being more focal in the former case concerning, especially, the lateral localization accuracy; with $q = 1$, the activity is more clearly limited to the left

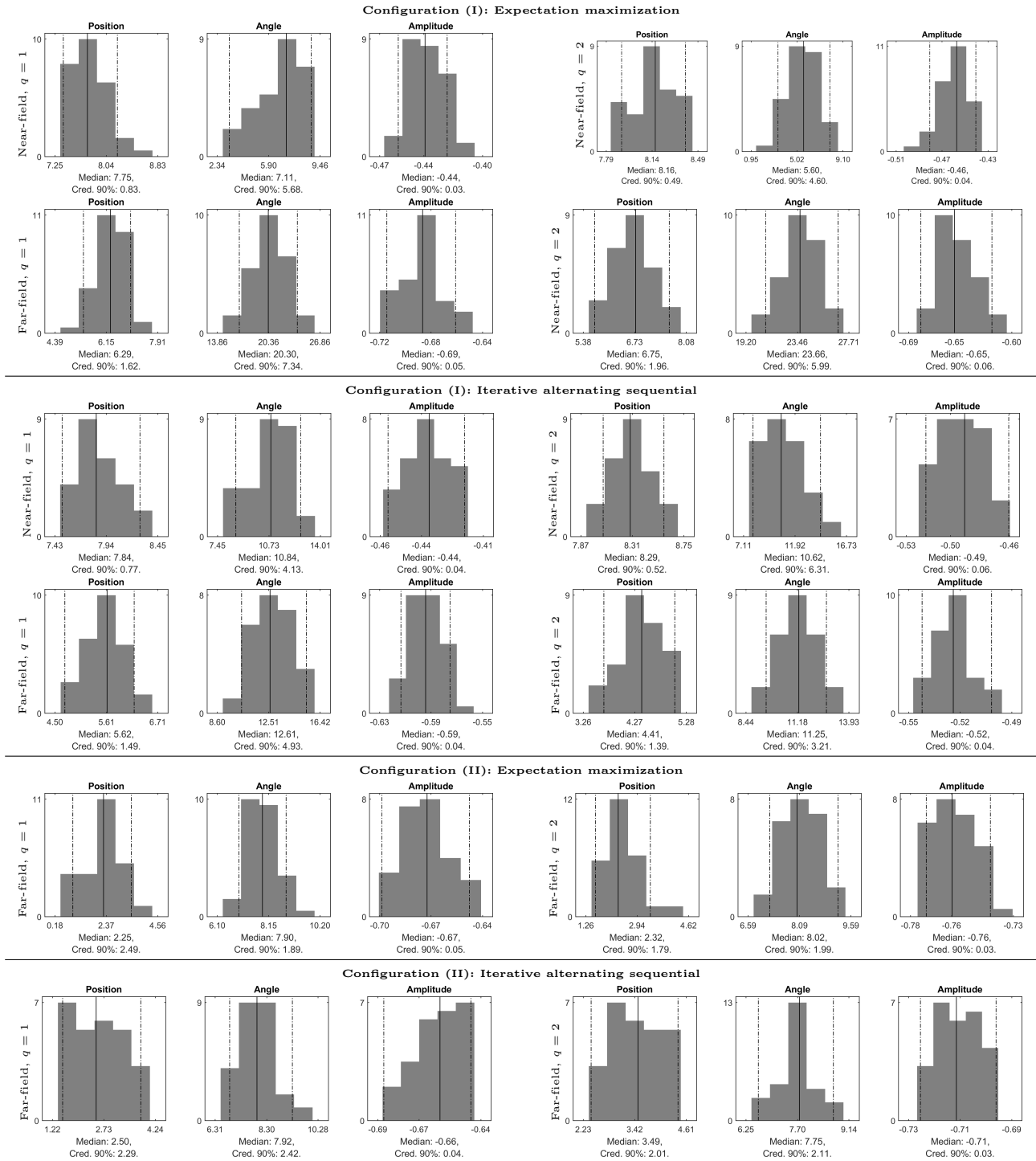


Fig. 8: The source localization accuracy measures (position, angle and amplitude) which are evaluated in the spherical Ary model with 5 % noise for source configurations (I) and (II) from Section 3.3.1 by applying the EM and IAS algorithm. The histograms are as in Figure 3.

lobe of the thalamus, whereas with $q = 2$, both lobes show activity.

As shown by the histograms, the results obtained with 5 % noise are generally of lower quality compared to those corresponding to 3 %. Considering the

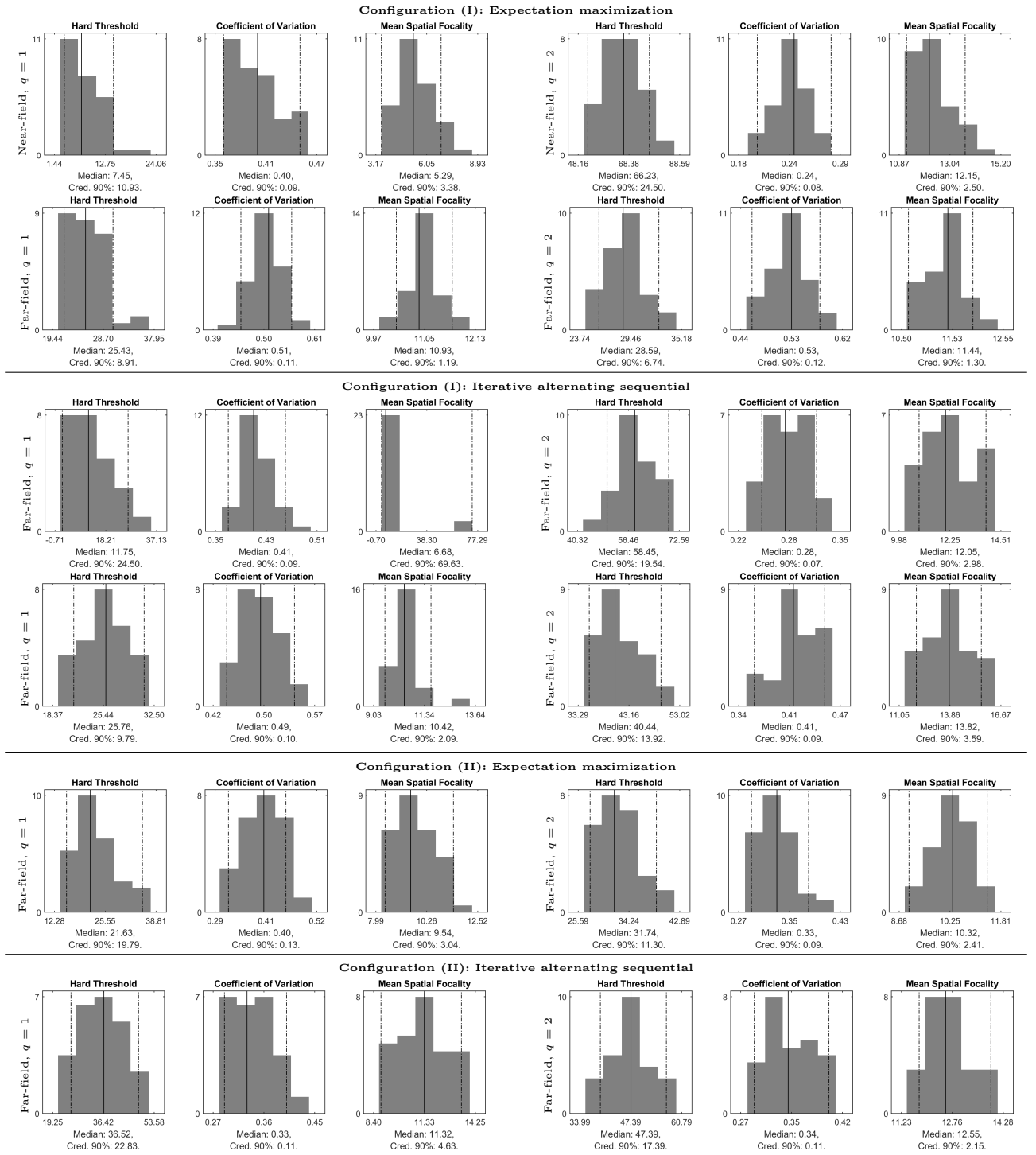


Fig. 9: The focality measures evaluated in the spherical Ary model with 5 % noise (Section 3.2.1) for source configuration (I) and (II), determined on Section 3.3.1, by applying the EM and IAS algorithm. The histograms are as in Figure 4.

MRI-based head model, the focality of the estimates obtained with $q = 1$ maintains pronounced compared to the case of $q = 2$ with the 5 % noise level. Moreover,

EM yields a superior reconstruction of the simultaneous cortical and deep activity of P20/N20 compared to the IAS algorithm. Since the histograms for the el-

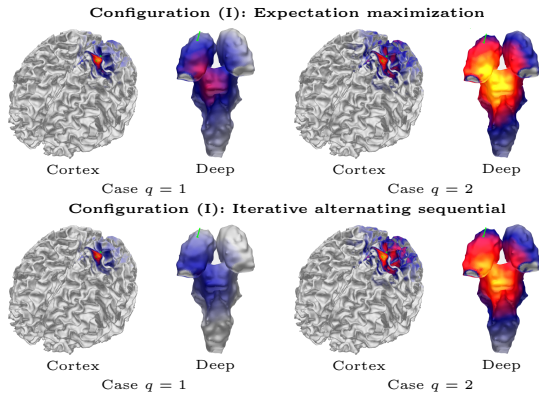


Fig. 10: The reconstructions obtained with 5 % noise and the MRI-based head multi-compartment model for source configuration **(I)** including two sources, one placed in the left 3b Brodmann area of the central sulcus, pointing inwards in the direction of the local surface normal vector, and a vertical source placed in the ventral posterolateral part of the left thalamus (Figure 1). The actual source position is visualized by a green pointer in each image.

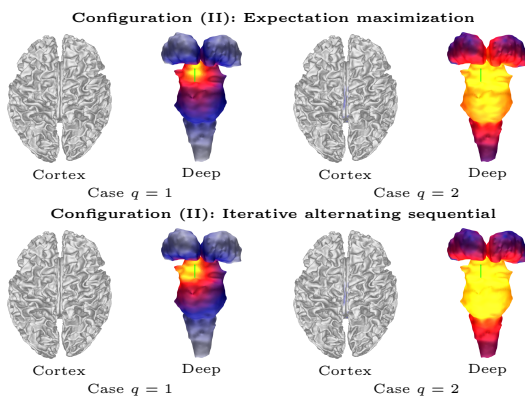


Fig. 11: The reconstructions obtained with 5 % noise and the MRI-based head multi-compartment model for source configuration **(II)**, including a single deep source placed in the brainstem (green pointer).

evated noise do not suggest significant differences between EM and IAS, we deem that these observations might be due to the increased overall level of uncertainty.

5 Discussion

In this paper, we interpreted the previously introduced conditionally Gaussian source (CGP) model [8] as a special case of the conditionally exponential prior (CEP) and compared these two priors in the numerical exper-

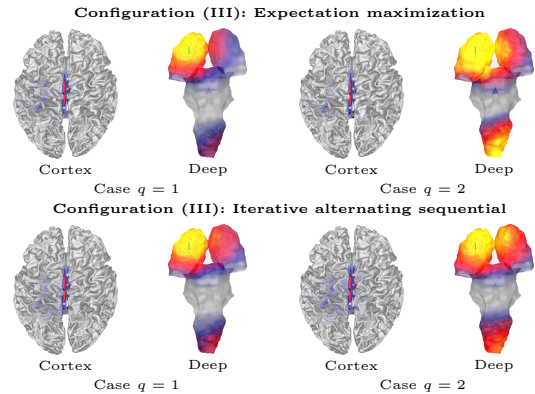


Fig. 12: The reconstructions obtained with 5 % noise and the MRI-based head multi-compartment model for source configuration **(III)** with a quadrupolar deep source formed by two dipolar components, one in the ventral part of the left thalamus [7] and another one in lower medulla of the brainstem [19] (green arrows).

iments using two different reconstruction techniques: the expectation maximization (EM) and iterative alternating sequential (IAS) algorithm. The EM and IAS reconstruction approaches were shown to update the expectation of the prior variance based on the mean and mode of the conditional posterior distribution, respectively. The source localization performance obtained with EM and IAS is close to similar with 3 % noise while with 5 % noise the EM reconstructions were found to be superior in reconstructing the simultaneous cortical and deep activity associated with P20/N20. Our results, however, suggest that, these findings rather reflect the overall increased noise effects than a significant performance difference in MAP estimation between EM and IAS. Furthermore, it was shown (Appendix A) that for the second-degree CEP, i.e., the case of prior degree $q = 2$, the EM and IAS algorithm differ only by the constant shape and scale parameter value κ and θ determining the CEP.

The performance of the CEP was analyzed numerically using both the spherical three-compartment Ary model and an MRI-based multi-compartment model. The first one of these was applied in quantitative accuracy and focality analysis, and the second one in a qualitative investigation, especially, to learn about the possible physiological relevance of the reconstruction difference. The EM and IAS method were im-

plemented in the context of RAMUS in order to enable the simultaneous detection of both cortical and sub-cortical activity. In particular, as shown in section 3.3, this combination allows selecting the source-wise shape and scale parameter of the hyperprior through the physiological properties of the brain activity [25, 16]. This combination omits the group effects following from a single focal activity being associated with multiple densely distributed sources. This is possible, since in RAMUS, the initial reconstruction is first found for a coarse and randomly distributed set of sources (here a set of 10 source positions) and after that propagated towards a denser distribution of sources. If this is not the case, the scale parameters needs to be adjusted based on the density of the source space: the greater the source space size the smaller the scale [18].

To reconstruct the far-field components optimally regardless of the electrode positioning, a method such as RAMUS is required to apply the source sparsity technique [31, 20]. It can be applied with various source localization methods, since it is rather a source space decomposition method than a reconstruction approach itself, averaging out errors that follow from the numerical discretization. However, based on the present results, it is evident that RAMUS tends to spread the far-field components, if this tendency is not taken into account *a priori*. CEP seems to provide a potential alternative for limiting the spread that occurs with CGP, while CGP can still be regarded advantageous for distinguishing activity, when multiple sources are simultaneously active.

When coupled with RAMUS, the CEP was found to localize deep activity with both prior degrees $q = 1$ and $q = 2$. Based on the results, the source localization performance provided by the first-order prior can be seen crucial for the focal detection of both near- and far-field activity. In the case $q = 1$, the near-field fluctuations (cortical patterns) in configuration (I) as well as the far-field (thalamic and sub-thalamic) components in (II) and (III) were observed to be more concentrated to their actual positions which is potentially significant regarding the identification of the ac-

tivity with the corresponding brain regions. With configuration (II) involving simultaneous near- and far-field activity, the deep activity obtained with $q = 1$, was slightly deviated with respect to the actual position, following obviously from the difficulty to recover a weakly-detectable deep component in the presence of the near-field activity. This difference is, nevertheless, minor in the case of the MRI-based head model which distinguishes the sub-cortical areas as disentangled compartments. Overall, the EM and IAS methods were found to provide qualitatively similar results.

The combination of the first-degree CEP and RAMUS constitutes a potential technique for localizing focal sources with limited distinguishability, e.g., SEP-origimators. Those are classically observed via invasive depth electrodes, i.e., stereo-EEG, in order to improve the visibility of the weak components. The present results suggest overall that non-invasive measurements might be successfully used to detect focal deep sources via efficient source localization strategy, e.g., the CEP. The feasibility of detecting deep activity non-invasively has been shown recently [33, 29]. The studies concerning the originators of the median nerve SEPs [3, 7, 6, 19] associate a significant uncertainty with the early far-field components. Of the median nerve SEP components, the clearest visibility has been obtained for P14/N14 considered as an example case here. P14/N14 is observed when the median nerve SEP propagates within the brainstem. The components P16/N16, modelled in this study, and P18/N18 occurring 16 and 18 ms post-stimulus, respectively, are likely to involve more than one deep originators and there is yet no exact knowledge on the actual location of those. The P20/N20 component, also considered here, is the first one involving cortical activity the presence of which, if not taken into account appropriately, might hinder detecting the simultaneous deep propagation. Based on our results, the originators of the P14/N14, P16/N16 and P20/20 component might be non-invasively detectable. Furthermore, the identification of these might be enhanced with the first-degree CEP ($q = 1$). Obviously, the detectability of different SEP originators will need to be care-

fully studied further both via numerical simulations and with experimental data in order to gain a deeper insight into the practical applicability of the CEP.

The present source localization approach provides a potential solution for investigating the function and connectivity of the neural activity networks with focal and weakly detectable far-field components, the analysis of the SEP originators being only one example of the potential applications. The present reconstruction techniques are distributional. In RAMUS, each stage of the investigated reconstruction process concerns a fixed, even though randomized, distribution of source positions. As these are not moving, the forward model (1) can be maintained linear at each stage. The final reconstruction is found as a linear superposition of multiple reconstructions obtained for randomized source sets. It approximates the actual primary current density of the neural activity. In this regard, the reconstruction process can be interpreted to average out the discretization and other modelling errors related to the linear forward model [31]. An alternative approach is to apply a non-linear source localization process involving an arbitrary number of moving dipolar sources. To improve the distinguishability of the brain activity, for example, filtering of particle clouds can be applied which is the approach of, e.g., the SESAME (SEquential Semi-Analytic Monte-carlo Estimation) technique [34]. Such a filtering approach carries a similarity to the present randomization process, motivating a potential future comparison between particle filtering based source localization and RAMUS with the goal to find out the common aspects and differences between the dipolar and distributional source localization approaches. For such a study the first-degree CEP, providing the best possible source localization focality with RAMUS, would be a natural choice.

6 Conclusion

This paper introduced CEP as a means to enhance the focality of the reconstructions in the localization of near- and far-field sources in EEG based on the

combined HBM and RAMUS. This combination was shown to allow selecting the shape and scale parameter of the hyperprior relying on a typical brain activity and measurement amplitude, incorporating the noise level due to different uncertainty factors, e.g., measurement and forward modelling errors. We observed that the first-degree CEP can improve the focality compared to the second-degree case which corresponds to the previously introduced CGP. This improvement was found to be significant especially in the reconstruction of both near- and far-field sources, e.g., to distinguish activity in the thalamus simultaneously with a source in the or a dipolar or quadrupolar source configuration focally in the brainstem. These findings are crucial, for example, in reconstructing and analyzing SEPs, e.g., the originators of the P20/N20, P14/N14 and P16/N16 component of the median nerve SEP, respectively.

Acknowledgments

AR, and SP were supported by the Academy of Finland Centre of Excellence in Inverse Modelling and Imaging 2018–2025. AR was also supported by the Vilho, Yrjö and Kalle Väisälä Foundation. AK was supported by the Academy of Finland Postdoctoral Researcher grant number 316542.

A Iterative alternating sequential algorithm

Here we present the standard forms of the iterative alternating sequential (IAS) algorithm (as appeared in [8] for a conjugate hyperprior). In particular, the IAS solves the MAP estimate $(\mathbf{x}^{(\text{MAP})}, \boldsymbol{\theta}^{(\text{MAP})}) = \arg \max \{\pi(\mathbf{x}, \boldsymbol{\theta} \mid \mathbf{y})\}$ as follows :

1. Set $\boldsymbol{\theta} = \boldsymbol{\theta}^{(0)}$ for $j = 0$;
2. Update \mathbf{x} by solving $\mathbf{x}^{j+1} = \arg \max \{\pi(\mathbf{x} \mid \mathbf{y}, \boldsymbol{\theta}^{(j)})\}$;
3. Update $\boldsymbol{\theta}$ by considering $\boldsymbol{\theta}^{(j+1)} = \arg \max \{\pi(\boldsymbol{\theta} \mid \mathbf{y}, \mathbf{x}^{(j+1)})\}$; if the hyperprior is conjugate, then

$$\theta_i^{(j+1)} = \left(\theta + \frac{(x_i^{(j+1)})^2}{2} \right) / (\kappa + 3/2) \quad \text{for } i = 1, \dots, n. \quad (11)$$

4. Set $j = j + 1$ and continue from 2 until it converges.

A.1 Correspondence of the model parameters and their effect on the optimization problems

Two different approaches are introduced to find the MAP using the CEP as a prior in (6) and (10). For the conditional Gaussian prior and inverse gamma hypermodel (IG-CG), the alternating optimization problem can be presented analytically as follows

$$\theta_i^{(j+1)} = \frac{|x_i^{(j)}|^2 / 2 + \theta}{\kappa + 3/2}, \quad (12)$$

$$\mathbf{x}^{(j+1)} = \arg \min_{\mathbf{x}} \left\{ \frac{1}{2\sigma^2} \|\mathbf{L}\mathbf{x} - \mathbf{y}\|_2^2 + \frac{1}{2} \|\mathbf{D}_\theta^{-1/2} \mathbf{x}\|_2^2 \right\},$$

where $\mathbf{D}_\theta = \text{diag}(\theta_1, \dots, \theta_n)$. The introduced problem have shape parameters κ and scale parameter θ for the IG hyperprior. Considering the case where the parameter $q = 2$ and comparing CEP's diagonal matrix \mathbf{D}_γ and the conditionally Gaussian one \mathbf{D}_θ , one can obtain $\gamma_i = \frac{1}{2\theta_i}$, for every diagonal element¹. Hence, the MAP estimate solved using the EM, when the CEP prior (2) has $q=2$, results in the same estimates as the IAS (that solves the above mentioned IG-CG model) when the CEP parameters κ and θ are set equal to $\kappa + 1$ and 2θ respectively. Moreover, by setting κ to $\kappa + 2$ and θ to 2θ in the iterative scheme (10), we conclude to the above mentioned IG-CG modelling solved by IAS. Thereby, the standard IG-CG is included in the CEP modelling when $q=2$.

B Solving the Lasso problem via Expectation Maximization

Here we revisit the sparsity constraint problem (also referred to as Lasso problem) [35] and we explain how it can be solved using Expectation Maximization (EM) [23, 14, 15]. The Lasso problem [35] is to solve

$$\hat{\mathbf{x}} := \arg \min_{\mathbf{x}} \left\{ \frac{1}{2\sigma^2} \|\mathbf{L}\mathbf{x} - \mathbf{y}\|_2^2 + \sum_{i=1}^n \gamma_i |x_i| \right\}, \quad (13)$$

where γ_i are fixed tuning parameters. In a similar expression as in (13), we can conclude following the Bayesian framework. Given the Gaussian likelihood function of the form $\exp(-\frac{1}{2\sigma^2} \|\mathbf{L}\mathbf{x} - \mathbf{y}\|_2^2)$ and the Laplace prior $\pi(\mathbf{x}) = \prod_{i=1}^N \pi(x_i)$, where

$$\pi(x_i) = \text{Lap}(x_i; 0, 1/\gamma_i) = \frac{\gamma_i}{2} \exp(-\gamma_i |x_i|) \quad (14)$$

Thereby, we have that the maximum a posteriori (MAP) estimation obtained via Bayes' rule is equivalent to the Lasso problem (13). Using the previous decomposition and denoting $\mathbf{w}^2 = (w_1^2, \dots, w_n^2)$, we can apply the Expectation Max-

imization (EM) algorithm [14, 11] to solve iteratively the optimization problem

$$\mathbf{x}^{(j+1)} := \arg \max_{\mathbf{x}} \{ \mathbb{E}_{\pi(\mathbf{w}^2 | \mathbf{x}^{(j)})} [\log(\pi(\mathbf{y} | \mathbf{x}) \pi(\mathbf{x} | \mathbf{w}^2) \pi(\mathbf{w}^2))] \}. \quad (15)$$

The above optimization problem can be represented in the form

$$\mathbf{x}^{(j+1)} := \arg \min_{\mathbf{x}} \left\{ \frac{1}{2\sigma^2} \|\mathbf{L}\mathbf{x} - \mathbf{y}\|_2^2 + \sum_{i=1}^n \frac{1}{2} x_i^2 \mathbb{E}_{\pi(w_i^2 | x_i^{(j)})} [w_i^2] \right\}. \quad (16)$$

The expectation (E) step of EM is given by $\mathbb{E}_{\pi(w_i^2 | x_i^{(j)})} [w_i^2] = \int_0^\infty w_i^2 \pi(w_i^2 | x_i^{(j)}) dw_i^2$. We can use the Bayes' rule for $\pi(w_i^2 | x_i)$ to show that

$\mathbb{E}_{\pi(w_i^2 | x_i^{(j)})} [w_i^2] = \frac{\gamma_i}{|x_i^{(j)}|}$. That is why, we solve the minimization problem

$$\mathbf{x}^{(j+1)} := \min_{\mathbf{x}} \left\{ \frac{1}{2\sigma^2} \|\mathbf{L}\mathbf{x} - \mathbf{y}\|_2^2 + \sum_{i=1}^n \frac{\gamma_i}{2|x_i^{(j)}|} x_i^2 \right\} \quad (17)$$

which is the maximization (M) step (i.e. point estimate for \mathbf{x}). For unimodal posterior we set $\gamma_i = \gamma_i/\sigma$ in (17) [28].

References

1. Baumgärtner, U., Vogel, H., Ohara, S., Treede, R.D., Lenz, F.A.: Dipole source analyses of early median nerve sep components obtained from subdural grid recordings. *Journal of neurophysiology* **104**(6), 3029–3041 (2010)
2. Braess, D.: *Finite Elements*. Cambridge University Press, Cambridge (2001)
3. Buchner, H., Adams, L., Knepper, A., Rüger, R., Laborde, G., Gilsbach, J.M., Ludwig, I., Reul, J., Scherg, M.: Preoperative localization of the central sulcus by dipole source analysis of early somatosensory evoked potentials and three-dimensional magnetic resonance imaging. *Journal of neurosurgery* **80**(5), 849–856 (1994)
4. Buchner, H., Adams, L., Müller, A., Ludwig, I., Knepper, A., Thron, A., Niemann, K., Scherg, M.: Somatotopy of human hand somatosensory cortex revealed by dipole source analysis of early somatosensory evoked potentials and 3d-nmr tomography. *Electroencephalography and Clinical Neurophysiology/Evoked Potentials Section* **96**(2), 121–134 (1995)
5. Buchner, H., Fuchs, M., Wischmann, H.A., Dössel, O., Ludwig, I., Knepper, A., Berg, P.: Source analysis of median nerve and finger stimulated somatosensory evoked potentials: multichannel simultaneous recording of electric and magnetic fields combined with 3d-mr tomography. *Brain topography* **6**(4), 299–310 (1994)

¹ In effect, γ are the precision weights and θ are the prior variances

6. Buchner, H., Knoll, G., Fuchs, M., Rienäcker, A., Beckmann, R., Wagner, M., Silny, J., Pesch, J.: Inverse localization of electric dipole current sources in finite element models of the human head. *Electroencephalography Clin Neurophysiol.* **102**(4), 267–78 (1997)
7. Buchner, H., Waberski, T., Fuchs, M., Wischmann, H.A., Beckmann, R., Rienäcker, A.: Origin of p16 median nerve sep component identified by dipole source analysis—subthalamic or within the thalamo-cortical radiation? *Experimental brain research* **104**(3), 511–518 (1995)
8. Calvetti, D., Hakula, H., Pursiainen, S., Somersalo, E.: Conditionally gaussian hypermodels for cerebral source localization. *SIAM Journal on Imaging Sciences* **2**(3), 879–909 (2009). DOI 10.1137/080723995
9. Calvetti, D., Pascarella, A., Pitolli, F., Somersalo, E., Vantaggi, B.: Brain activity mapping from meg data via a hierarchical bayesian algorithm with automatic depth weighting. *Brain topography* pp. 1–31 (2018)
10. Calvetti, D., Somersalo, E.: *An Introduction to Bayesian Scientific Computing: Ten Lectures on Subjective Computing*, vol. 2. Springer Science & Business Media (2007)
11. Caron, F., Doucet, A.: Sparse bayesian nonparametric regression. In: *Proceedings of the 25th international conference on Machine learning - ICML 08*. ACM Press (2008). DOI 10.1145/1390156.1390168
12. Creutzfeldt, O.D., Fromm, G.H., Kapp, H.: Influence of transcortical dc currents on cortical neuronal activity. *Experimental neurology* **5**(6), 436–452 (1962)
13. Dannhauer, M., Lanfer, B., Wolters, C.H., Knösche, T.R.: Modeling of the human skull in EEG source analysis. *Human Brain Mapping* **32**, 1383–1399 (2011). DOI 10.1002/hbm.21114
14. Figueiredo, M.: Adaptive sparseness for supervised learning. *IEEE Transactions on Pattern Analysis and Machine Intelligence* **25**(9), 1150–1159 (2003). DOI 10.1109/tpami.2003.1227989
15. Griffin, J., Brown, P.: Bayesian adaptive lassos with non-convex penalization. *ResearchGate* (2007)
16. Hämäläinen, M., Hari, R., Ilmoniemi, R.J., Knuutila, J., Lounasmaa, O.V.: Magnetoencephalography — theory, instrumentation, and applications to invasive studies of the working human brain. *Reviews of Modern Physics* **65**, 413–498 (1993)
17. Haueisen, J., Leistriz, L., Süsse, T., Curio, G., Witte, H.: Identifying mutual information transfer in the brain with differential-algebraic modeling: evidence for fast oscillatory coupling between cortical somatosensory areas 3b and 1. *NeuroImage* **37**(1), 130–136 (2007)
18. He, Q., Rezaei, A., Pursiainen, S.: Zeffiro user interface for electromagnetic brain imaging: a gpu accelerated fem tool for forward and inverse computations in matlab. *Neuroinformatics* pp. 1–14 (2019)
19. Hsieh, C.L., Shima, F., Tobimatsu, S., Sun, S.J., Kato, M.: The interaction of the somatosensory evoked potentials to simultaneous finger stimuli in the human central nervous system. a study using direct recordings. *Electroencephalography and Clinical Neurophysiology/Evoked Potentials Section* **96**(2), 135–142 (1995)
20. Krishnaswamy, P., Obregon-Henao, G., Ahveninen, J., Khan, S., Babadi, B., Iglesias, J.E., Hämäläinen, M.S., Purdon, P.L.: Sparsity enables estimation of both subcortical and cortical activity from meg and eeg. *Proceedings of the National Academy of Sciences* **114**(48), E10465–E10474 (2017)
21. Miinalainen, T., Rezaei, A., Us, D., Nüßing, A., Engwer, C., Wolters, C.H., Pursiainen, S.: A realistic, accurate and fast source modeling approach for the eeg forward problem. *NeuroImage* **184**, 56–67 (2019)
22. de Munck, J., Wolters, C.H., Clerc, M.: EEG & MEG forward modeling. In: R. Brette, A. Destexhe (eds.) *Handbook of Neural Activity Measurement*. Cambridge University Press, New York (2012). DOI 10.1017/CBO9780511979958.006
23. Murphy, K.P.: *Machine Learning*. MIT Press Ltd (2012). URL https://www.ebook.de/de/product/19071158/kevin_p_murphy_machine_learning.html
24. Nadarajah, S.: A generalized normal distribution. *Journal of Applied statistics* **32**(7), 685–694 (2005)
25. Niedermeyer, E., da Silva, F.L.: *Electroencephalography: Basic Principles, Clinical Applications, and Related Fields*, Fifth Edition. Lippincott Williams & Wilkins, Philadelphia (2004)
26. Noël, P., Ozaki, I., Desmedt, J.E.: Origin of n18 and p14 far-fields of median nerve somatosensory evoked potentials studied in patients with a brain-stem lesion. *Electroencephalography and clinical neurophysiology* **98**(2), 167–170 (1996)
27. O’Hagan, A., Forster, J.J.: *Kendall’s advanced theory of statistics, volume 2B: Bayesian inference, vol. 2*. Arnold (2004)
28. Park, T., Casella, G.: The bayesian lasso. *Journal of the American Statistical Association* **103**(482), 681–686 (2008). DOI 10.1198/016214508000000337
29. Pizzo, F., Roehri, N., Villalon, S.M., Trébuchon, A., Chen, S., Lagarde, S., Carron, R., Gavaret, M., Giussiano, B., McGonigal, A., et al.: Deep brain activities can be detected with magnetoencephalography. *Nature communications* **10**(1), 971 (2019)
30. Pursiainen, S., Vorwerk, J., Wolters, C.: Electroencephalography (EEG) forward modeling via H(div) finite element sources with focal interpolation. *Physics in Medicine and Biology* **61**(24), 8502–8520 (2016). DOI 10.1088/0031-9155/61/24/8502
31. Rezaei, A., Koulouri, A., Pursiainen, S.: Randomized multiresolution scanning in focal and fast e/meg sensing of brain activity with a variable depth. *Brain Topography* pp. 1–15 (2020)

-
32. Rullmann, M., Anwander, A., Dannhauer, M., Warfield, S.K., Duffy, F.H., Wolters, C.H.: Eeg source analysis of epileptiform activity using a 1 mm anisotropic hexahedra finite element head model. *NeuroImage* **44**(2), 399–410 (2009)
 33. Seeber, M., Cantonas, L.M., Hoevels, M., Sesia, T., Visser-Vandewalle, V., Michel, C.M.: Subcortical electrophysiological activity is detectable with high-density eeg source imaging. *Nature communications* **10**(1), 753 (2019)
 34. Sommariva, S., Sorrentino, A.: Sequential monte carlo samplers for semi-linear inverse problems and application to magnetoencephalography. *Inverse Problems* **30**(11), 114020 (2014)
 35. Tibshirani, R.: Regression shrinkage and selection via the lasso. *Journal of the Royal Statistical Society: Series B* **58**, 267–288 (1994)